Dispersion control of broadband super–Rayleigh speckles for snapshot spectral ghost imaging

Pengwei Wang (王鹏威)[1,2], Zhentao Liu (刘震涛)[1,2,*], Jianrong Wu (吴建荣)[1], Xia Shen (沈 夏)[1], and Shensheng Han (韩申生)[1,2,3]

[1] Key Laboratory of Quantum Optics, Shanghai Institute of Optics and Fine Mechanics, Chinese Academy of Sciences, Shanghai 201800, China

[2] Center of Materials Science and Optoelectronics Engineering, University of Chinese Academy of Sciences, Beijing 100049, China

[3] Hangzhou Institute for Advanced Study, University of Chinese Academy of Sciences, Hangzhou 310024, China

Snapshot spectral ghost imaging, which can acquire dynamic spectral imaging information in the field of view, has attracted increasing attention in recent years. Studies have shown that optimizing the fluctuation of light fields is essential for improving the sampling efficiency and reconstruction quality of ghost imaging. However, the optimization of broadband light fields in snapshot spectral ghost imaging is challenging because of the dispersion of the modulation device. In this study, by judiciously introducing a hybrid refraction/diffraction structure into the light-field modulation, snapshot spectral ghost imaging with broadband super-Rayleigh speckles was demonstrated. The simulation and experiment results verified that the contrast of speckles in a broad range of wavelengths was significantly improved, and the imaging system had superior noise immunity.

Keywords: spectral imaging; ghost imaging; dispersion.
DOI: 10.3788/COL202220.091102

1. Introduction

Spectral imaging acquires a three-dimensional (3D) spectral data cube, in which additional spectral information contains a significant amount of object information. It plays an important role in many applications, such as astronomical imaging, remote sensing, and biomedical imaging[1,2]. In contrast to conventional spectral imaging, which requires time scanning along either the spatial or wavelength axis, snapshot spectral imaging acquires a 3D spectral data cube in a single exposure[3,4]. Depending on whether reconstruction is required, snapshot spectral imaging can be divided into computational snapshot spectral imaging and non-computational snapshot spectral imaging. Integral field spectrometry with faceted mirrors (IFS-M)[5], multi-aperture filtered camera (MAFC)[6], and image-replicating imaging spectrometer (IRIS)[7] are representative methods of non-computational snapshot spectral imaging. Meanwhile, computational snapshot spectral imaging[8–13] usually modulates the spatial and spectral information of an object by light-field spatial intensity fluctuation and reconstructs the 3D spectral data cube information from the detected intensity light distribution. With the development of computational snapshot spectral imaging via light-field amplitude modulation[8], the use of light-field phase modulation to achieve spatial intensity fluctuation has

also made considerable progress in computational snapshot spectral imaging[9–13]. For example, spectral ghost imaging modulates the image in the entire spectral band by utilizing a spatial random phase modulator, and the spectral images of the object are obtained by second-order spatial mutual light-field correlation[11].

Meanwhile, research has shown that optimizing the speckle light field can significantly improve the sampling efficiency and the reconstruction quality of ghost imaging, especially at low signal-to-noise ratios (SNRs) and low sampling rates[14–17]. Recently, there has been interest in generating speckles with tailored intensity statistics[18–20]. Bromberg et al. developed a simple method for producing non-Rayleigh speckles by redistributing the intensity among the speckle grains with a phase-only (P) spatial light modulator (SLM)[18]. Furthermore, they developed a general method for customizing the speck intensity statistics[19]. Liu et al. proposed a method for generating super-Rayleigh speckles based on the principle of light reversibility and demonstrated snapshot spectral ghost imaging with a super-Rayleigh modulator[20]. However, to the best of our knowledge, unlike the Rayleigh speckles statistical characteristics, which do not change with wavelength, the non-Rayleigh speckles statistical characteristics suffer from dispersion in the broad-spectrum band. Therefore, the optimization of broadband light fields in

snapshot spectral ghost imaging is challenging because of modulation device dispersion.

In this study, by introducing a hybrid refraction/diffraction structure, we propose a method for generating super-Rayleigh speckles over a broad range of wavelengths. The design theory of dispersion control for broadband super-Rayleigh speckles was derived and verified through simulations and experiments. The experimental imaging results showed that the reconstruction quality of snapshot spectral ghost imaging with broadband super-Rayleigh speckles was significantly improved, especially in the case of a low SNR.

2. Theory and Simulation

2.1. Theory

As shown in Fig. 1, an object is imaged on the first imaging plane by a lens, and the SLM modulates light from the first imaging plane 'b,' resulting in a light intensity distribution on the speckle plane 'd' to be detected by a CCD. The amplitude and phase (AP) distribution of the SLM is designed to generate super-Rayleigh speckles $w(\mathbf{r}_1) = U_{\text{Ray}}(\mathbf{r}_1)^n$ on the speckle plane 'd' by Liu et al.'s method[20], where $U_{\text{Ray}}(\mathbf{r}_1)$ is a Rayleigh speckle distribution, and n is chosen as positive integers. Based on the principle of light reversibility, the light field in the SLM plane can be expressed as

$$U_{\text{slm}}(\mathbf{r}_0, \lambda_0)$$
$$= \frac{j}{\lambda_0 z_2} \exp\left(-j\frac{2\pi}{\lambda_0} z_2\right) \int_{-\infty}^{\infty} w(\mathbf{r}_1) \exp\left[-j\frac{\pi}{\lambda_0 z_2}(\mathbf{r}_0 - \mathbf{r}_1)^2\right] d\mathbf{r}_1, \tag{1}$$

where z_2 is the distance between the SLM and virtual speckle plane 'c,' λ_0 is the wavelength, and $\mathbf{r}_0$ and $\mathbf{r}_1$ represent the two-dimensional coordinates in the SLM plane and the virtual speckle plane 'c,' respectively.

When the lens of focal length f is achromatic, objects with different wavelengths λ are imaged to the same first imaging plane 'b,' and the light field in the speckle plane 'd' generated by the point source on the first imaging plane 'b' is calculated as
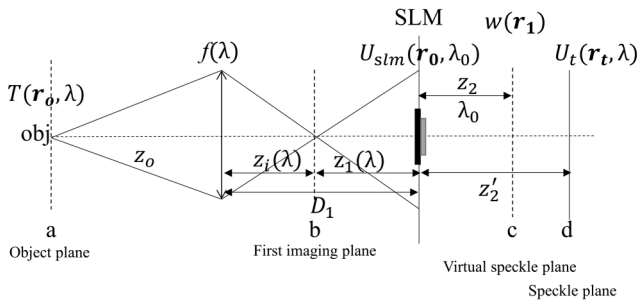
Fig. 1. Schematic of snapshot spectral ghost imaging with broadband super-Rayleigh speckles. (a) is the object plane; (b) is the first imaging plane; (c) is the virtual speckle plane; (d) is the speckle plane.

$$U_t(\mathbf{r}_t, \lambda) = \frac{1}{j\lambda z_2'} \exp\left(j\frac{2\pi}{\lambda} z_2'\right) \int U_0(\mathbf{r}_0, \lambda) U_{\text{slm}}(\mathbf{r}_0, \lambda_0)$$
$$\times \exp\left[j\frac{\pi}{\lambda z_2'}(\mathbf{r}_t - \mathbf{r}_0)^2\right] d\mathbf{r}_0, \tag{2}$$

where $U_0(\mathbf{r}_0, \lambda)$ is the light field before the SLM, z_2' is the distance between the SLM plane and speckle plane, and $\mathbf{r}_t$ represents the two-dimensional coordinates of the speckle plane. The contrast of the light field $U_t(\mathbf{r}_t, \lambda)$ is

$$C = 1 + \frac{\sum_{k=1}^{n-1} \frac{(C_n^k)^4 [k!(n-k)!]^2}{(n!)^2}}{1 + \frac{k(n-k)z_2^2 \lambda^2 \left[\beta - \frac{1}{(\gamma+\tau)}\right]^2}{\pi^2 \sigma^4}}, \tag{3}$$

where $\gamma = \frac{z_2}{z_2'}, \tau = \frac{z_2}{z_1}, \beta = \frac{\lambda_0}{\lambda}, z_1$ is the distance between the first imaging plane and the SLM plane, C_n^k is a combination symbol, which means a combination of n things taken k at a time, and σ is the standard deviation of the Gaussian distribution satisfied by the autocorrelation of Rayleigh speckles $U_{\text{Ray}}(\mathbf{r}_1)$ in the virtual speckle plane. When $\beta = \frac{1}{\gamma+\tau}$ is satisfied, namely

$$z_1 = \left(\frac{\lambda}{\lambda_0 z_2} - \frac{1}{z_2'}\right)^{-1}, \tag{4}$$

the contrast C in Eq. (3) reaches the maximum,

$$C_{\max} = 1 + \frac{\sum_{k=1}^{n-1} (C_n^k)^4 [k!(n-k)!]^2}{(n!)^2}. \tag{5}$$

From Eqs. (4) and (5), the speckle contrast reaches a maximum at different planes depending on the wavelength λ, which is consistent with the dispersion effect in traditional diffractive lens imaging systems[21]. Thus, by controlling the lens' dispersion to compensate for the dispersion effect of the modulation through the SLM, we can maintain a high contrast of the speckle pattern over a wide wavelength range.

A series of achromatic methods has been developed to compensate for dispersion in traditional diffractive imaging[22–24]. Based on the hybrid refraction/diffraction structure achromatic principle, a refractive lens of focal length f is used for dispersion compensation. Because imaging using a refractive lens satisfies

$$\frac{1}{z_o} + \frac{1}{z_i} = \frac{1}{f}, \tag{6}$$

substituting Eq. (4) into Eq. (6), we have

$$f = \left(\frac{1}{z_o} + \frac{1}{D_1 - \frac{z_2 \beta}{1-\gamma\beta}}\right)^{-1}, \tag{7}$$

where z_o is the object distance. Then, the intensity distribution of the speckle behind the SLM with a distance z_2' can be expressed as

$$I(\mathbf{r}_t, \lambda) \propto w\left(\beta\gamma\mathbf{r}_t - \beta\frac{z_i}{z_o}\tau\mathbf{r}_o\right)w^\star\left(\beta\gamma\mathbf{r}_t - \beta\frac{z_i}{z_o}\tau\mathbf{r}_o\right), \quad (8)$$

where $w^\star$ denotes the light distribution function of a super-Rayleigh speckle on the virtual speckle plane, and $\mathbf{r}_o$ represents the two-dimensional coordinates in the object plane. Equation (8) shows that the speckles with different wavelengths on the speckle plane 'd' are just a scaling of the initial super-Rayleigh speckles on the virtual speckle plane 'c' with a scale factor $\beta\gamma = \frac{\lambda_0 z_2}{\lambda z_2'}$. The contrast of speckles does not change with wavelength and reaches C_{max} in Eq. (5).

The spatial resolution is determined by the correlation function of the speckles generated by two points at the same wavelength and different positions with a distance $\Delta\mathbf{r}_o$[11],

Fig. 2. Numerical simulation results for the speckle contrast varied with the system parameters z_1, z_2', and λ. (a) The simulation results of the speckle contrast varied with the system parameters z_1 and λ. Here, z_2' = 10.6 mm. (b) The simulation results of the speckle contrast varied with the system parameters z_2' and λ. Here, z_1 = 60 mm. The solid black line is the theoretical curve based on Eq. (4).

$$\gamma(\Delta\mathbf{r}_o) = \frac{(n!)^2 \exp[-n(B\Delta\mathbf{r}_o)^2] + \sum_{k=1}^{n-1}(C_n^k)^4[k!(n-k)!]^2 \exp[-(n-k)(B\Delta\mathbf{r}_o)^2]}{(n!)^2 + \sum_{k=1}^{n-1}(C_n^k)^4[k!(n-k)!]^2}, \quad (9)$$

where $B = \beta\tau\frac{z_i}{z_o\sigma}$, and the spectral resolution can be determined by the correlation function of the speckles generated by two points at the same position and different wavelengths with a gap $\Delta\lambda$[11],

$$\gamma(\Delta\lambda) \approx \frac{(n!)^2 \exp[-n(D\mathbf{r}_t\Delta\lambda)^2] + \sum_{k=1}^{n-1}(C_n^k)^4[k!(n-k)!]^2 \exp[-(n-k)(D\mathbf{r}_t\Delta\lambda)^2]}{(n!)^2 + \sum_{k=1}^{n-1}(C_n^k)^4[k!(n-k)!]^2}, \quad (10)$$

where $D = \frac{\lambda_0 z_2}{\lambda\lambda' z_2'\sigma}$. As shown in the subsequent experimental results, this has almost the same spectral and spatial resolution as traditional snapshot spectral ghost imaging.

2.2. Simulation

To verify the results of the theoretical derivation, we carried out a numerical simulation based on the Fresnel diffraction formula. First, we generated a random phase matrix uniformly and randomly distributed between 0 and 2π and used it as the phase applied to SLM. Then, the Rayleigh speckles in the virtual plane were obtained by the free propagation of the light field. The field of the super-Rayleigh speckle in the virtual speckle plane was obtained by numerically raising the value of the Rayleigh speckles in the virtual speckle plane to the power $n = 3$. Then, by inversely propagating the field of the super-Rayleigh speckle in the virtual speckle plane with a distance $z_2 = 9$ mm at a wavelength $\lambda_0 = 650$ nm, the AP distribution of the obtained light field was extracted to the SLM. According to the Fresnel diffraction formula, we simulated the light field on the speckle plane generated by a point source at different z_1, z_2', and λ on the first imaging plane. Figure 2 shows that the simulated speckle contrast varies with the system parameters z_1, z_2', and λ, and the corresponding system parameters for maximum contrast satisfy Eq. (4).

Then, we set the simulation parameters in Fig. 1 as follows: $z_o = 100$ mm, $D_1 = 160$ mm, and $z_2' = 10.6$ mm. The simulated
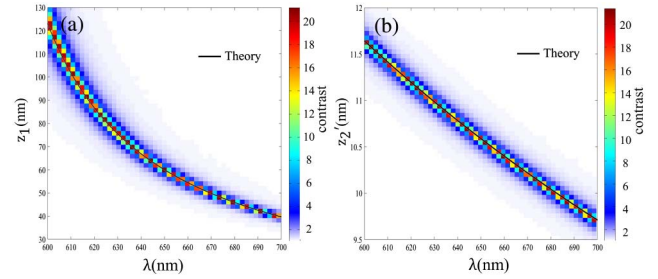
dispersion characteristic of the lens with focal length f satisfied Eq. (7). The AP and P distributions of $U_{slm}(\mathbf{r}_0,\lambda_0)$ were extracted to the SLM. By placing a source on the object plane, the light field on the speckle plane was simulated by the diffractive propagation of the light field under two cases of SLM with AP and P distributions, as shown in Fig. 3(a). This indicated that in the case of SLM with AP distribution, the generated speckles maintain the same super-Rayleigh distribution, as shown in Fig. 3(b), and the contrast of speckles with different wavelengths satisfied the theoretical results in Eq. (5). As shown in Fig. 3(c), in the case of SLM with P distribution, the contrast of the generated speckles is lower than in the case of SLM with AP distribution. However, it remained much higher than that of the Rayleigh speckles. We also simulate the case of the lens with focal length f as achromatic and SLM with AP and P modulation, as shown in Fig. 3(c). The simulated result showed that the contrast of the speckles was equal to the above-mentioned cases at the center wavelength and decreased as the wavelength deviated from the center wavelength [the brown and green lines in Fig. 3(c)]. The correlation functions of the speckles generated by two points at the same wavelength and different positions with a distance $\Delta\mathbf{r}_o$, and of the speckles generated by two points at the same position and different wavelengths with a gap $\Delta\lambda$, are shown in Figs. 3(d) and 3(e), respectively. The simulation results (blue line) were consistent with the theoretical results (dotted black line) in Eqs. (9) and (10).
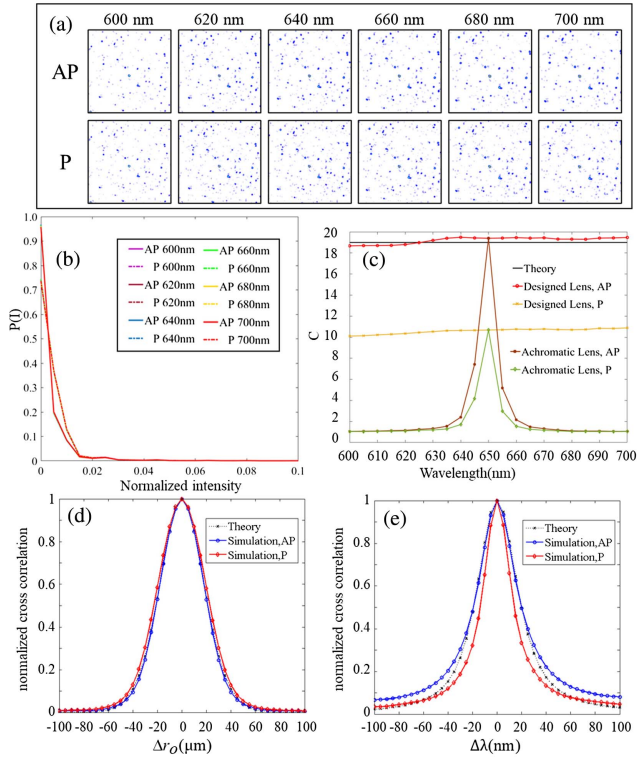
Fig. 3. (a) Simulation speckles of different wavelengths on the detection plane. AP: the amplitude and phase of U_{slm} (r_0, λ_0) were extracted to the SLM. P: the phase-only of U_{slm} (r_0, λ_0) was extracted to the SLM. (b) Probability distribution of the normalized intensity of the speckles. (c) Simulation results of the speckle contrast when the dispersion of the lens satisfied Eq. [7] (marked as designed lens), and the lens of focal length f was achromatic (marked as achromatic lens). The theoretical curve, according to Eq. [5], is also represented with the black line. (d) Theoretical curve and simulated curve of the correlation function for speckles generated by two points at the same wavelength and different positions with a distance Δr_0. (e) Theoretical and simulated curves of the correlation function of the speckles generated by two points at the same position and different wavelengths with a gap $\Delta\lambda$.

In addition, the contrast of the generated speckles was also affected by other non-ideal factors [such as the bandwidth ($\Delta\lambda$), size (Δx) of the calibration source, modulation size (D_{SLM}), fill factor, pixel size (Δp_{SLM}) of the SLM, the phase quantization level of the SLM, the aperture of the imaging lens, the pixel size (Δp_{CCD}) of the CCD, speckle magnification of lens 3, and stray light]. When these factors in the actual experiment were considered in the simulation (such as the calibration source's bandwidth $\Delta\lambda = 5$ nm, the calibration source's size $\Delta x = 20$ μm, the SLM's fill factor 0.95, the SLM's pixel size $\Delta p_{\text{SLM}} = 9.2$ μm, the SLM's phase quantization level of 256, lens 1's aperture $d_1 = 50.8$ mm, lens 2's aperture $d_2 = 50.8$ mm, lens 3's aperture $d_3 = 25.4$ mm, the speckles' magnification by lens 3 $\rho = 2$, the pixel size of the CCD $\Delta p_{\text{CCD}} = 3.45$ μm, and 1% stray light), the simulated speckles' contrast of $n = 3$ reduced from 19 to 1.28, and the simulated speckles' contrast of $n = 8$ reduced from 12,869 to 4.23. We noted that different values of n affected

the speckle contrast and the phase loaded on the SLM, but they did not affect dispersion compensation [shown in Eq. (7)]. To obtain better imaging quality, we increased the value of n in the actual experiment to increase the contrast of the experimental speckle.

3. Experimental Results

Figure 4(a) shows the experimental setup for snapshot spectral ghost imaging with broadband super-Rayleigh speckles. According to Eq. (7), the parameters for generating the phase matrix were set as $\lambda_0 = 400$ nm, $z_2 = 5$ mm, and $n = 8$. The parameters of the experimental system were set as $z_0 = 500$ mm, $D_1 = 155$ mm, and $z_2' = 10.6$ mm. The dispersion curves of the lens used in the experiment were calculated by importing the corresponding lens structure data into the optical design software, as shown in Fig. 4(b). The dispersion of Lens 2 [the red line in Fig. 4(b)] almost coincided with the theoretical curve according to Eq. (7) [black line in Fig. 4(b)]. The achromatic doublet lens (Lens 1) with a focal length of 500 mm (GCL-010611) and the K9 doubly convex lens (Lens 2) with a focal length of 150 mm (GCL-010212) formed a lens group to image objects of different wavelengths to different positions in front of the reflective SLM (1920 × 1152 meadowlark optics, pixel size was 9.2 μm × 9.2 μm, and fill factor was 95.7%). To achieve P modulation of the SLM, the light from the object passes through a polarizer (GCL-050003), whose polarization direction was consistent with that of the SLM with P modulation. A broadband
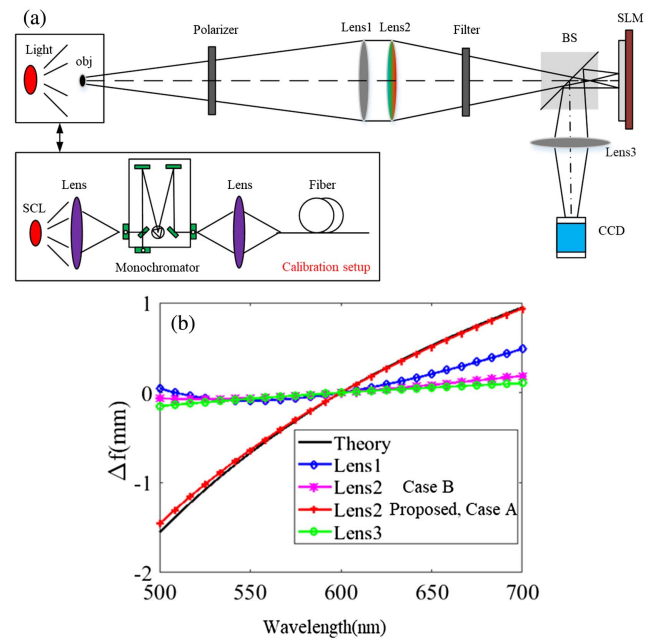
Fig. 4. (a) Experimental setup of the snapshot spectral ghost imaging with broadband super-Rayleigh speckles. The calibration setup shown in the bottom box was adopted instead of the object in the black box when calibrating. The SCL was a supercontinuum laser. (b) Dispersion curves of lenses used in the experiment.

bandpass filter of 500–700 nm (#84-743, #86-103, Edmund) was placed behind Lens 2. After being reflected by the SLM and the beam splitter with a beam splitting ratio of $R{:}T{=}1{:}1$, the light was magnified by an achromatic doublet lens (Lens 3) with a focal length of 30 mm (GCL-010650), the magnification is $\rho = 2$, and it was finally recorded by the CCD (Basler ace acA4112-30 µm).

Before the imaging process, a calibration process was required to obtain the intensity impulse response functions by scanning along the spatial and spectral dimensions using a monochromatic point source within the field of view (FOV)[11]. The calibration setup is shown in the black box at the bottom of Fig. 4(a). A monochromator (WDG30-Z, Beijing Optical Instrument Factory, Beijing, China) was illuminated by a supercontinuum laser (YSL-SC-PRO-7, YLS Photonics Inc., Wuhan, China) to produce quasi-monochromatic light and then coupled into an optical fiber with a diameter of 20 µm to produce a quasi-monochromatic point light source. Then, the point light source scanned 80×80 pixels at an interval of 40 µm within the FOV, and the wavelength was set in the monochromator scans from 500 nm to 700 nm at an interval of 20 nm.

In the imaging process, the intensity distribution I_t in the detection plane was regarded as an incoherent superposition of the intensity distributions generated by all points in the object plane. The image of the object can be obtained by calculating the second-order intensity correlation between the calibrated speckle patterns I_r and the imaging intensity distribution I_t in a single shot. The second-order correlation function $\Delta G^{(2)}$ is expressed as[11]

$$\Delta G^{(2)}(\boldsymbol{r}_r, \lambda_k) = \langle \Delta I_t(\boldsymbol{r}_t) \Delta I_r(\boldsymbol{r}_t; \boldsymbol{r}_r, \lambda_k) \rangle \propto T(\boldsymbol{r}_r, \lambda_k) \otimes g^{(2)}(\boldsymbol{r}_r, \lambda_k),$$
$$(11)$$

where $\langle \cdots \rangle$ is the ensemble average, $\boldsymbol{r}_r$ and $\boldsymbol{r}_t$ are the coordinate on the object plane and the detection plane, respectively, and $g^{(2)}(\boldsymbol{r}_r, \lambda_k)$ is the normalized second-order correlation function. $T(\boldsymbol{r}_r, \lambda_k)$ denotes the spectral images of objects with wavelength λ_k. Also, λ_k represents the kth spectral channel, and $\otimes$ denotes the operation of convolution.

Meanwhile, the imaging process can be expressed as[11]

$$Y = AX, \qquad (12)$$

where Y is an $M \times 1$ column vector obtained by reshaping the detected intensity, A is an $M \times (N \times L)$ measurement matrix, whose column vector is the calibrated speckle intensity, and X is an $(N \times L) \times 1$ column vector reshaped by the object's spectral images. N is the number of pixels in the spatial image, and L is the number of spectral channels. The spectral images were reconstructed by solving Eq. (12). Here, the TV-RANK algorithm was applied, which exploits the sparsity of the scene image and the low-rank constraint for multi-spectral images[25]. We also demonstrated the experimental results of conventional snapshot spectral ghost imaging with Rayleigh speckles and non-dispersion compensated snapshot spectral ghost imaging with super-Rayleigh speckles. In the experiment of the

conventional snapshot spectral ghost imaging with Rayleigh speckles, Lens 2 was still the K9 doubly convex lens with a focal length of 150 mm (GCL-010212), and the phase matrix loaded on the SLM was a random phase matrix uniformly and randomly distributed between 0 and 2π, which is denoted as Case A. In the experiment of non-dispersion compensated snapshot spectral ghost imaging with super-Rayleigh speckles, the phase matrix loaded on the SLM was still the customized phase, but Lens 2 was an achromatic doublet lens with a focal length of 150 mm (GCL-010616), which is denoted as Case B. The correlation functions of the experimental speckles generated by two points at the same wavelength and different positions with a distance Δr_o and of the experimental speckles generated by two points at the same position and different wavelengths with a gap $\Delta\lambda$, are shown in Figs. 5(a) and 5(b), respectively. The experimental results show that the spatial and spectral resolutions in the three cases were almost the same.

Figure 5(c) shows the experimental speckles of snapshot spectral ghost imaging with broadband super-Rayleigh speckles at different wavelengths. The experimental results demonstrate a scaling relationship between the speckles of snapshot spectral ghost imaging with broadband super-Rayleigh speckles at different wavelengths. Unlike non-dispersion compensated snapshot spectral ghost imaging with super-Rayleigh speckles, where the speckle contrast decreases as the wavelength deviates from the central wavelength, the broadband super-Rayleigh speckles modulation was realized, and the speckle contrast maintained a high level across the entire spectrum.
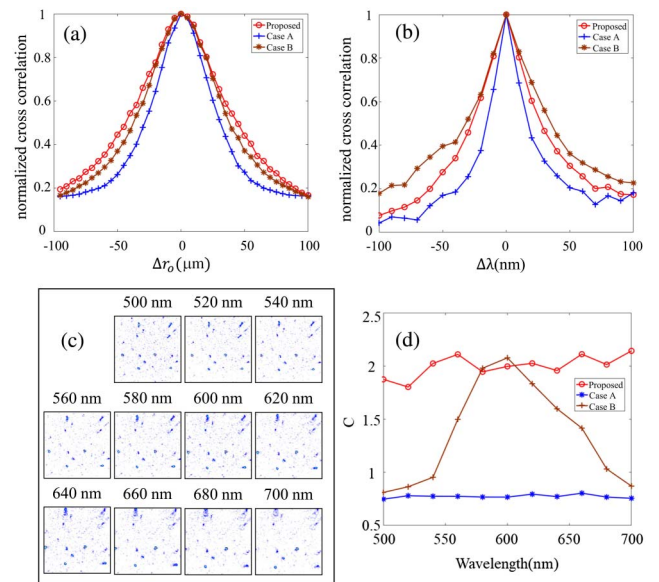

Fig. 5. (a) Curve of the correlation function of the experimental speckles generated by two points at the same wavelength and different positions with a distance Δr_o. (b) Curve of the correlation function of the experimental speckles generated by two points at the same position and different wavelengths with a gap $\Delta\lambda$. (c) The experimental speckles of snapshot spectral ghost imaging with broadband super-Rayleigh speckles at different wavelengths. (d) The contrast of speckles of the corresponding groups.

Fig. 6. Experimental imaging results with different exposure times, while the sampling rate remained at 40%. The mPSNR and mSSIM are also shown. (a) Exposure time of 50 ms. (b) Exposure time of 10 ms.

A transmissive butterfly target (shown in the first column of Fig. 6) was illuminated by a xenon lamp. Different SNRs, obtained by exposing 50 ms and 10 ms at a sampling rate of 40%, were demonstrated. To quantitatively analyze the quality of the reconstructed images, we calculated the peak SNR (PSNR) and the structural similarity index (SSIM)[26] for each wavelength compared with the corresponding reference images and obtained the mean PSNR (mPSNR) and mean SSIM (mSSIM) by averaging SSIM/PSNR with different wavelengths. As shown in Fig. 6, in the case of a high SNR with an exposure of 50 ms, the mPSNR of snapshot spectral ghost imaging with broadband super-Rayleigh speckles is 7 dB higher than that of the conventional snapshot spectral ghost imaging with Rayleigh speckles and 4 dB higher than that of non-dispersion compensated snapshot spectral ghost imaging with super-Rayleigh speckles. In addition, the mSSIM of the imaging results of the snapshot spectral ghost imaging with broadband super-Rayleigh speckles is also significantly higher than that of the two above-mentioned snapshot spectral ghost imaging. In the case of low SNR with an exposure of 10 ms, conventional snapshot spectral ghost imaging with Rayleigh speckles no longer imaged the target, and non-dispersion compensated snapshot spectral ghost imaging with super-Rayleigh speckles only imaged the target near the center wavelength, while the snapshot spectral ghost imaging with broadband super-Rayleigh speckles still could image the target in a broad range of wavelengths. These experimental results demonstrated that snapshot spectral ghost imaging with broadband super-Rayleigh speckles had an excellent anti-noise ability.

4. Conclusion

In conclusion, we theoretically derived the dispersion condition for realizing broadband super-Rayleigh speckle modulation. Moreover, we verified this by implementing broadband super-Rayleigh speckles in simulations and experiments. The experimental imaging results indicated the noise immunity of snapshot spectral ghost imaging with super-Rayleigh speckles, and its imaging quality was significantly improved. In this paper, we experimentally achieved dispersion control at 500–700 nm. This wavelength range is mainly determined by the system parameters and the selected component dispersion. Since this paper mainly verifies the feasibility of the scheme in principle, the dispersive lens was first selected, and then the parameters of the modulation system were set according to its dispersion. In practical applications, the parameters of the modulation system are generally determined according to the spatial resolution, spectral resolution, and other system indices. The dispersive lens is then customized according to the Eq. (7), and its fit will limit the final dispersion compensation range. We expect this to be applied in low SNR spectral imaging scenarios such as microscopy[27], remote sensing[1], astronomy[28], medicine[2], and other fields.

References

1. A. F. H. Goetz, G. Vane, J. E. Solomon, and B. N. Rock, "Imaging spectrometry for earth remote sensing," Science **228**, 1147 (1985).
2. T. Vo-Dinh, B. Cullum, and P. Kasili, "Development of a multi-spectral imaging system for medical applications," J. Phys. D **36**, 1663 (2003).
3. N. Hagen and M. W. Kudenov, "Review of snapshot spectral imaging technologies," Opt. Eng. **52**, 090901 (2013).
4. L. Gao and L. V. Wang, "A review of snapshot multidimensional optical imaging: measuring photon tags in parallel," Phys. Rep. **616**, 1 (2016).
5. I. S. Bowen, "The image-slicer a device for reducing loss of light at slit of stellar spectrograph," Astrophys. J. **88**, 113 (1938).
6. A. Hirai, T. Inoue, K. Itoh, and Y. Ichioka, "Application of multiple-image Fourier transform spectral imaging to measurement of fast phenomena," Opt. Rev. **1**, 205 (1994).
7. A. R. Harvey and D. W. Fletcher-Holmes, "High-throughput snapshot spectral imaging in two dimensions," Proc. SPIE **4959**, 46 (2003).
8. G. R. Arce, D. J. Brady, L. Carin, H. Arguello, and D. S. Kittle, "Compressive coded aperture spectral imaging: an introduction," IEEE Signal Process. Mag. **31**, 105 (2014).
9. S. K. Sahoo, D. Tang, and C. Dang, "Single-shot multispectral imaging with a monochromatic camera," Optica **4**, 1209 (2017).
10. X. Li, J. A. Greenberg, and M. E. Gehm, "Single-shot multispectral imaging through a thin scatterer," Optica **6**, 864 (2019).
11. Z. Liu, S. Tan, J. Wu, E. Li, X. Shen, and S. Han, "Spectral camera based on ghost imaging via sparsity constraints," Sci. Rep. **6**, 25718 (2016).
12. K. Monakhova, K. Yanny, N. Aggarwal, and L. Waller, "Spectral DiffuserCam: lensless snapshot hyperspectral imaging with a spectral filter array," Optica **7**, 1298 (2020).
13. Z. Li, J. Suo, X. Hu, C. Deng, J. Fan, and Q. Dai, "Efficient single-pixel multispectral imaging via non-mechanical spatio-spectral modulation," Sci. Rep. **7**, 41435 (2017).
14. C. Wang, W. Gong, X. Shao, and S. Han, "The influence of the property of random coded patterns on fluctuation-correlation ghost imaging," J. Opt. **18**, 065703 (2016).
15. L. Zhang, Y. Lu, D. Zhou, H. Zhang, L. Li, and G. Zhang, "Superbunching effect of classical light with a digitally designed spatially phase-correlated wavefront," Phys. Rev. A **99**, 063827 (2019).
16. Y. Wang, F. Wang, R. Liu, P. Zhang, H. Gao, and F. Li, "Sub-Rayleigh resolution single-pixel imaging using Gaussian- and doughnut-spot illumination," Opt. Express **27**, 5973 (2019).
17. X. Liu, M. Li, X. Yao, W. Yu, G. Zhai, and L. Wu, "High-visibility ghost imaging from artificially generated non-Gaussian intensity fluctuations," AIP Adv. **3**, 52121 (2013).
18. Y. Bromberg and H. Cao, "Generating non-Rayleigh speckles with tailored intensity statistics," Phys. Rev. Lett. **112**, 213904 (2014).
19. N. Bender, H. Yılmaz, Y. Bromberg, and H. Cao, "Customizing speckle intensity statistics," Optica **5**, 595 (2018).

20. S. Liu, Z. Liu, C. Hu, E. Li, X. Shen, and S. Han, "Spectral ghost imaging camera with super-Rayleigh modulator," Opt. Commun. **472**, 126017 (2020).
21. D. C. O'Shea, T. J. Suleski, A. D. Kathman, and D. W. Prather, *Diffractive Optics: Design, Fabrication, and Test* (SPIE, 2004).
22. F. L. Pedrotti, L. M. Pedrotti, and L. S. Pedrotti, *Introduction to Optics*, Vol. **91** (Prentice-Hall, 1954).
23. T. Stone and N. George, "Hybrid diffractive-refractive lens and achromats," Appl. Opt. **27**, 2960 (1988).
24. G. Blough and G. M. Morris, "Hybrid lens offer high performance at low cost," Laser Focus World **31**, 67 (1995).
25. S. Tan, Z. Liu, E. Li, and S. Han, "Hyperspectral compressed sensing based on prior images constrained," Acta Opt. Sin. **35**, 0811003 (2015).
26. Z. Wang, A. C. Bovik, H. R. Sheikh, and E. P. Simoncelli, "Image quality assessment: from error visibility to structural similarity," IEEE Trans. Image Process. **13**, 600 (2004).
27. W. Li, Z. Tong, K. Xiao, Z. Liu, and Z. Wang, "Single frame wide-field nanoscopy based on ghost imaging via sparsity constraints (GISC nanoscopy)," Optica **6**, 1515 (2019).
28. P. C. Agrawal, "A broad spectral band Indian Astronomy satellite 'Astrosat'," Adv. Space Res. **38**, 2989 (2006).